



3D phase mapping of solid oxide fuel cell YSZ/Ni cermet at the nanoscale by holographic X-ray nanotomography

Villanova Julie ^a, Laurencin Jérôme ^{b,*}, Cloetens Peter ^a, Bleuet Pierre ^c, Delette Gérard ^b, Suhonen Heikki ^a, Usseglio-Viretta François ^b

^aESRF, 6 rue Jules Horowitz BP 220, 38043 Grenoble, France

^bCEA-Liten, MINATEC Campus, 17 rue des Martyrs, 38054 Grenoble Cedex 9, France

^cCEA, LETI, MINATEC Campus, 17 rue des Martyrs, 38054 Grenoble Cedex 9, France



HIGHLIGHTS

- Special X-ray nanotomography gives relevant 3D reconstructions of Ni–8YSZ.
- Two large volumes ($51.2 \times 25.6^2 \times \pi \mu\text{m}^3$) with high resolution (voxel size: 25 nm) were obtained.
- The 3 phases of the cermet are separated in the functional layer and the substrate.
- The resolution and representative volume element for such electrodes are discussed.

ARTICLE INFO

Article history:

Received 30 August 2012

Received in revised form

30 May 2013

Accepted 12 June 2013

Available online 20 June 2013

Keywords:

Solid oxide fuel cell

Ni/YSZ cermet

3D reconstruction

X-ray nanotomography

ABSTRACT

SOFC electrochemical performances are strongly dependent on the micro and nanostructure of the electrodes. 3D image analysis is an essential tool to characterise these microstructures. However, the studied volumes have to be sufficiently large to be representative of the heterogeneous medium. In this study, quantitative phase contrast X-ray nano-holotomography is performed on large volumes of SOFC anode consisting by a Ni/YSZ cermet. Both the electrode functional layer and the current collector of anode supported cell are characterised in 3D. The setup and data processing adaptation needed for such an absorbing materials are described. The X-ray nano-holotomography was performed with an isotropic voxel size of $25 \times 25 \times 25 \text{ nm}^3$ and a field of view of about 50 μm . This technique is non-destructive and was used in local tomography mode. After filtering and thresholding, the segmentation of the 3D reconstructions allows precisely separating the network of each phase of the electrode (metallic, ceramic and porosity), giving representative features of the microstructure.

© 2013 Elsevier B.V. All rights reserved.

1. Introduction

Many of the advanced materials currently being developed have complex multiscale structures that require physical and chemical understanding at the nanometer scale. In the field of energy production, fuel cells involve materials having a 3D architecture with features spanning from the micrometer down to the nanometer range. For those reasons fuel cells, that convert chemical into electrical energy, must ideally be observed with a probe able to give 3D insights deep into the materials and with the ability to reveal details of few nanometers. Among the different types of fuel cells, solid oxide fuel cells (SOFC) have the particularity of working at

high temperature (800 °C), which makes the tracking of the degradation phenomena even more critical. Their electrochemical and mechanical performances are directly linked to the nanostructure of their materials [1,2]. A typical fuel cell is a three-layered structure (Fig. 1(a) and (b)): one dense electrolyte of yttria stabilised zirconia (YSZ) between two porous electrodes [1]. A composite of Ni and YSZ is usually used as anode material. In the case of anode supported cells, the anode is divided into two layers: (i) a thick (between 500 μm and 1.5 mm) highly porous anodic substrate and (ii) a thin ($\sim 5\text{--}10 \mu\text{m}$) anode functional layer (AFL). The coarse microstructure of the anode substrate is crucial for the gas transportation whereas the finer microstructure of the AFL is optimised to increase the length of triple-phase boundaries (TPB) where the electrochemical reactions take place. Clearly, the electrochemical performances of SOFCs are inevitably linked to this multiscale architecture. A better understanding of this link is essential for the

* Corresponding author. Tel.: +33 4 38782210; fax: +33 4 38784139.

E-mail address: jerome.laurencin@cea.fr (L. Jérôme).

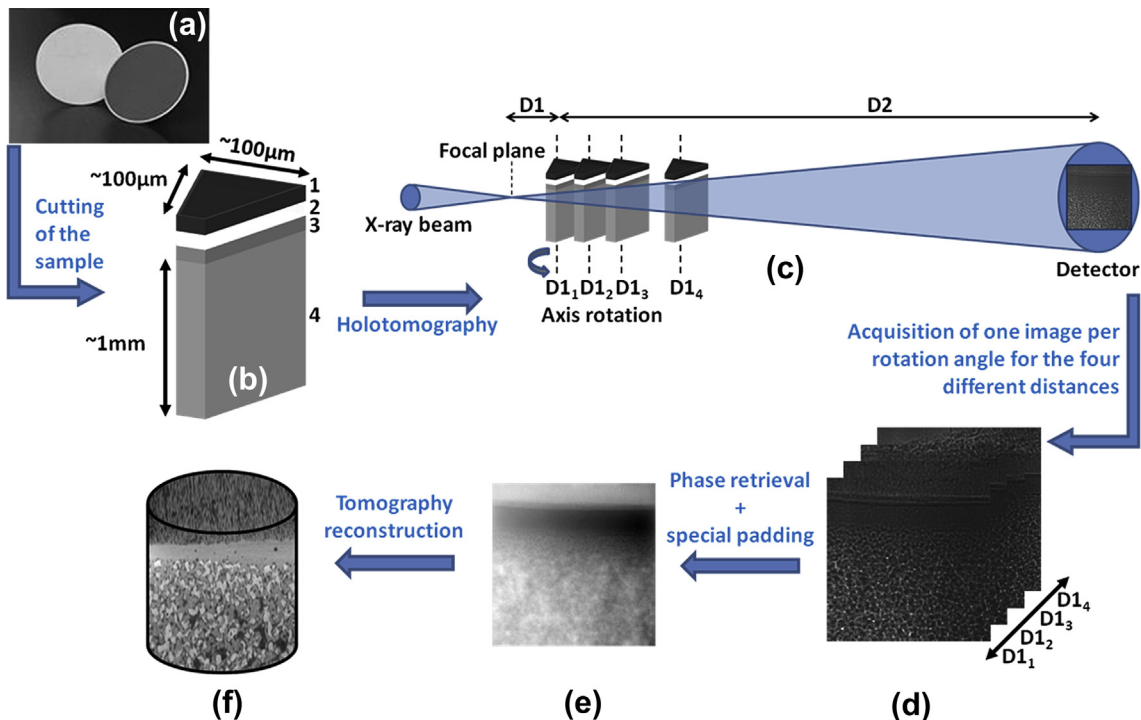


Fig. 1. Schematic representation of the different steps of the experiment. (a) Picture of the unit cells of SOFC. (b) Schematic representation of the sample cut such as: (1) cathode, (2) electrolyte, (3) AFL, (4) anode. (c) ID22NI holotomography experimental setup: the X-ray beam is focused down to 100 nm using KB mirrors. The detector system consists of a high efficiency LSO:Tb luminescent converter screen, lens coupled to a large dynamic range and highly efficient Charged-Coupled Device camera (ESRF developed FReLoN camera: 2048 × 2048 pixels). The distance between the focal plane and the detector is fixed at around 0.7 m. (d) Example of four different distances images. Here, the rotation angle is 0° and the pixel size is 25 nm. (e) Phase map reconstructed using the four different distances images at 0° with the phase retrieval method. The magnification of the phase map is equal to the one of the $D_{1,1}$ image. (f) 3D reconstruction of the sample.

design of optimised microstructures in order to improve the SOFC reliability and efficiency [3]. A challenging problem consists of performing numerical simulations based on an accurate representation of the media to describe some basic physical processes. Indeed, relevant effective material properties can be obtained by different homogenisation techniques. Furthermore, 3D image analysis can be repeated after different steps of cell operation to identify some degradation mechanisms.

Several studies have already linked the decrease of cell performances to the microstructure evolution of the anode [4–6]. Most of them take into account the 3D nature of SOFC which allows calculation of microstructural properties such as phase connectivity, phase tortuosity, and TPB length [7–11]. Two techniques are used for 3D nanocharacterization [12]: focused ion beam coupled with a scanning electron microscope (FIB–SEM) [13] and X-ray nanotomography [14]. For both techniques, the samples studied must be shaped to fit the experimental constraints. FIB–SEM is a time-consuming technique that gives high resolution (from 10 nm to 100 nm) but on relatively small volumes (around $10 \times 10 \times 10 \mu\text{m}^3$) [7,15,16]. Regarding the X-ray nanotomography, the differentiation between the nickel and the YSZ has been achieved doing absorption tomography across the Ni K-absorption edge (8.333 keV) [17–21]. With such a low X-ray energy, only small samples, around $10 \times 10 \times 10 \mu\text{m}^3$, could be studied with a voxel size of $22 \times 22 \times 22 \text{ nm}^3$.

The typical size of these reconstructions (around $10 \times 10 \times 10 \mu\text{m}^3$) [7,14,15,22] is not suitable for the study of the anode substrate because the representative volume element (RVE) to provide good statistics on effective transport properties is around $35 \times 35 \times 35 \mu\text{m}^3$ [23]. Nevertheless, some large samples have been reconstructed using FIB tomography, the largest one was achieved by Kanno et al. [24]: a volume of $45.8 \times 14.5 \times 26.2 \mu\text{m}^3$ with a

resolution of 55.8 nm/pixel on SEM images and with an FIB milling distances of 74.7 nm. The study of the AFL seems to require a smaller RVE [16,25], even if larger volumes are better for statistics [26]. However, the resolution should be high enough to describe accurately the fine microstructure of the AFL. For instance, a resolution of ~ 35 nm seems to be required to determine accurately its particle size distribution [11]. This makes SOFC characterisation challenging since it requests a 3D probe operating on large volumes, *i.e.* with a large penetration depth, and at high resolution. Electron probes do not fulfill simultaneously these requirements: electron tomography is far too local and FIB–SEM, which appears at first as a technique of choice, would take too much time to cover such a large volume. It is furthermore fully destructive, preventing all *in-situ* studies of the microstructure evolution. A radiation, which attenuation properties allow sufficiently penetrating bulk samples, must be used and hard X-rays are the best candidate. Unfortunately, there are no commercial X-ray tomography systems that operate at high resolution with high energy X-rays. Rather, systems providing high resolution use low energy X-rays [27], limiting the sample size to small volumes. Because of the brilliance of 3rd generation synchrotron X-ray sources, X-ray synchrotron tomography seems to be well suited for SOFC 3D nanocharacterization. A key point with respect to lab-based techniques is that hard X-rays are available, which allows 3D reconstruction of large volumes. From Fig. 2, an X-ray energy of at least 24 keV gives suitable attenuation for Ni/YSZ cermet samples whose cross-section is 100 μm . Prior studies performed on anode substrates at high energy (29 keV) have already allowed large reconstructions ($42 \times 42 \times 105 \mu\text{m}^3$) in which the porous network could be quantified [23]. However, in that study the differentiation between the Ni and the YSZ phases was not possible. Here, we propose a new methodology based on X-ray nano-holotomography that is a phase

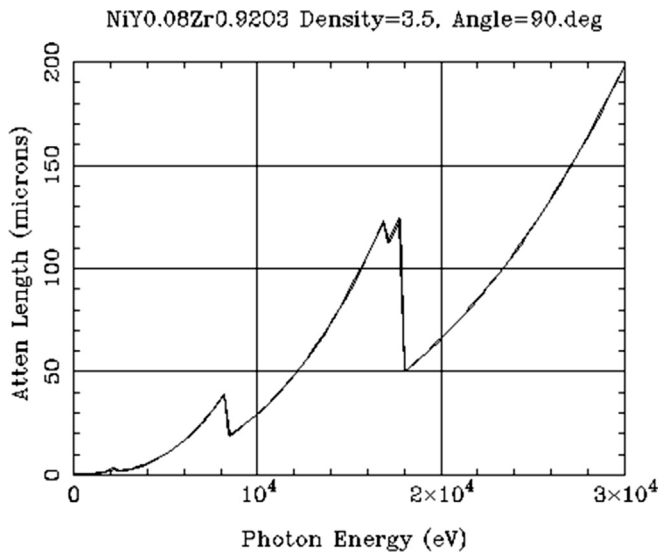


Fig. 2. X-ray attenuation length of Ni/YSZ cermet with 47% of porosity and 50 wt% of Ni and 50 wt% of YSZ (bulk density: 3.5).

contrast imaging technique, at high energy (i) to reconstruct large volumes with high resolution and (ii) to distinguish the 3 phases in both the Ni–YSZ substrate and the functional layer. Using these reconstructions, the effective properties of the porous electrodes could be determined with a high level of reliability.

2. Experimental details

2.1. Samples preparation

Commercial anode supported cells (ASCs) supplied by the Forschungszentrum Jülich (FZJ) research center [28] already used in a previous study [23] were used for the experiment. The anode layer is constituted of 50 wt% Ni and 50 wt% 8YSZ (ZrO₂ stabilised with 8 mol% Y₂O₃), with a ~1 mm thick substrate layer and a ~10 μm thin AFL layer. For the holotomography process described hereafter, samples must have a needle shape as depicted on Fig. 1(b). Great attention was paid to the machining method since samples are brittle due to the high porosity of the bulk material. They were all prepared before the reduction step.

Starting from a circular full cell of 56 mm diameter, strips of 1 mm width and ~20 mm length were laser cut in order to limit the polishing time. Then, strip widths are further decreased from 1 mm down to 100 μm by using a Gatan Centar Frontier polishing system from Gatan, Inc. The 100 μm strips are finally sawed along their length using wire cutting to obtain a needle whose thickness is equal to the full sheet thickness, i.e. the multi-layered structure is preserved for the X-ray tomography experiments. Due to some imperfections of the wire cutting device, the last step gives rise to needles whose cross-section appears to be triangular (a round or square shape would have been preferred to maximise the volume within the field of view). Some samples have been embedded into a specific resin (ref. E505, Epotecn®) with the aim of studying the effect on the phase retrieval procedure (see details below). It is worth mentioning that no damage induced by the beam has been observed during the experiments.

2.2. Adapting the nano-holotomography scheme to SOFCs

The holotomography method is a phase contrast imaging technique that has been developed for weakly absorbing specimens

such as the biological samples. This method is also adapted to study samples that present two different phases having a similar absorption. Imaging SOFCs with X-rays is challenging because SOFCs are highly absorbent materials and the specimens previously described still have a large cross-section for high resolution tomography. For that reason the conventional holotomography scheme had to be adapted, as described in this section.

The technique used is 3D nano-holotomography, that has been performed at the nano-imaging end station (ID22NI) of the European Synchrotron Radiation Facility ID22 beamline [29], following the holotomography principle [30,31]. The experimental setup is schematically shown on Fig. 1(c). Basically, a 29 keV synchrotron beam from an U23d undulator is first horizontally slit down to 25 μm to reduce the natural horizontal synchrotron source size. Then, the high harmonics are filtered out using the Pt stripe of a mirror. At 64 m away from the undulator source, the so-called “pink” beam is focused down to less than 100 × 100 nm² using Kirkpatrick Baez (KB) multilayer mirrors.

The focused beam is then used as a secondary X-ray source, which allows to record magnified X-ray nanoradiographs of the sample by suitably choosing the focus to sample distance (Fig. 1). However, those radiographs are significantly different from conventional radiographs based on X-ray tubes because of the spatial coherence of the synchrotron X-ray beam and because of the high spatial resolution achieved. The interaction of a coherent x-ray beam with matter affects both its amplitude and phase. This can be described by the complex refractive index n :

$$n = 1 - \delta + i\beta \quad (1)$$

The quantity β is linked to the linear attenuation coefficient μ and to the wavelength λ by $\mu = 4\pi\beta/\lambda$. It describes the well-known absorption contrast. The refractive index decrement δ is related to the phase shift and is given by:

$$\delta = \frac{r_c \lambda^2}{2\pi V} \sum_j (Z_j + f'_j) \quad (2)$$

where $r_c = 2.8$ fm is the classical electron radius. The summation is over all atoms contained in the representative volume V ; Z_j is their atomic number and f'_j the real part of the wavelength dependent dispersion correction [32]. The phase contrast is given by the changes in electronic density or, to a good approximation, by the changes in mass density.

Holotomography exploits the phase shift quantitatively and is usually relevant for low-Z materials, for example polymers and biological samples. Indeed, in these cases the absorption coefficient μ —that is mostly driven by the photoelectric effect at these energies and whose cross-section is proportional to Z^4 —becomes so small that there is no significant absorption contrast. Then, the ratio between δ and β is so big that the object behaves as a pure phase object. The radiographs are in this case dominated by propagation based phase contrast, with almost no absorption contrast. The phase contrast consists of interference fringes due to Fresnel diffraction. Therefore it is very different from an absorption projection and it can in this configuration not be used as input for a proper tomographic reconstruction.

Cloetens et al. [30] developed an approach to retrieve the phase quantitatively and come back to absorption-like images. The complete description of the acquisition principle and of data processing is beyond the scope of this paper and the reader can refer to [30,31]. Practically, it consists in acquiring four data sets at four focus to sample distances ($D_{11}, D_{12}, D_{13}, D_{14}$ —Fig. 1(c)). This four distance scheme is justified by the fact that a spatially coherent X-ray beam illuminating a phase object will extinct some spatial frequencies in

the projections, depending on the effective propagation distance [33]. Starting from these four data sets, a numerical scheme allows the optical phase to be retrieved giving a single absorption-like image at the highest magnification, corresponding to the distance D_{11} [30,31]. The phase is proportional to the projection of the refractive index decrement δ and can be used as input for a regular tomographic reconstruction.

For SOFCs, a first important point is to work with hard X-rays. Here, the energy is fixed to 29 keV to limit the absorption of a 100 μm thick sample of Ni/YSZ cermet and also to get better phase retrieval conditions. The average refractive index decrement δ at 29 keV of an SOFC composite made of 40 vol.% of Ni and 60 vol.% of YSZ is $\delta = 1.65 \times 10^{-6}$ while the corresponding absorption coefficient is $\beta = 3.844 \times 10^{-8}$. The refractive index decrement is about 43 times larger than the absorption coefficient: projections are neither pure phase images nor pure absorption images but rather a mix between the two. This forces us to adapt the holographic reconstruction to take into account the significant absorption. In brief, we determine a first estimate of the phase map using a Paganin like approach [34] and assuming a homogenous coefficient δ/β equal to 43. This estimate provides only a blurred version of the phase map. It is iteratively improved using a non-linear least squares optimisation. We used twenty iterations and removed the homogeneity assumption in the recursive part of the calculation. The phase retrieval conditions are further optimised by embedding samples into Epoxy resin. Indeed, the calculation method seems to reach its limits when the phase changes too rapidly, which can lead to significant errors in the measurement and image blurring. Since $\delta_{(\text{YSZ+Ni})} = 1.65 \times 10^{-6}$, $\delta_{\text{air}} = 0$ and $\delta_{\text{Epoxy}} = 4 \times 10^{-7}$, the phase shift between the SOFC matrix and the environment (i.e. air or Epoxy resin) can be reduced by a quarter by embedding SOFC samples into Epoxy resin.

In this study, the holotomography has been performed based on tomography scans with 1999 projections collected over 360° for each distance D_{1i} . The four distances have been chosen to reach a final pixel size of 25 nm ($D_{11} = 24$ mm, $D_{12} = 25$ mm, $D_{13} = 29$ mm, $D_{14} = 39$ mm). We can calculate the magnification M given by

$$M = \frac{D_1 + D_2}{D_1} \quad (3)$$

with D_1 the distance between the focal plane and the sample and D_2 the distance between the sample and the detector (Fig. 1(c)). In our case the focus to detector distance is fixed and equal to $D_1 + D_2 = 705$ mm. Selecting $D_{11} \approx 24$ mm gives $M = 30$. Taking into account this magnification and the detector pixel size of 0.75 μm the pixel size on the final image is indeed 25 nm. For a 2048 \times 2048 pixels detector the field of view is about 51 μm . This field of view is smaller than the sample cross-sections as described in the previous section. For that reason, a special padding scheme adapted to local tomography was developed. Padding (extending the acquired images outside the visible field of view) is important both for the phase retrieval procedure and the tomographic reconstruction. Doing it incorrectly would result in final reconstructions that show significant changes in the background and that are difficult to segment. The padding scheme takes into account the geometry of the sample cross-section. The latter is estimated from a coarse tomographic reconstruction of the fourth scan at D_{14} (largest field of view) with a reconstructed slice area artificially increased to 8192 \times 8192 pixels. This coarse reconstruction is nevertheless sufficient to distinguish areas with and without matter. From this estimate of the geometry of the sample cross-section and the average sample composition, radiographs can be calculated to pad the experimental images to a size of 4096 \times 4096 pixels. This padding is consistently used both for the phase retrieval

and the filtering part of the tomographic reconstruction (filtered backprojection algorithm). The phase retrieval was carried out with inhouse software using the GNU Octave programming environment (<http://www.octave.org>) and the public domain image analysis program ImageJ (<http://rsbweb.nih.gov/ij/>). Eventually, tomographic reconstruction using the filtered phase maps was performed using backprojection with the ESRF software PyHST.

2.3. Algorithm for image segmentation

Image segmentation by thresholding the grayscale histogram is an important step in the 3D image analysis. The threshold value has to be localised somewhere in the valley between two peaks of the gray-level histogram. If the valleys are broad and poorly defined, an approximate threshold can introduce artefacts in the segmentation. The proportion and distribution of each phase can be changed if they are miss-assigned. To tackle this shortcoming, a specialised methodology has been implemented in Matlab® software. The method is based on a prior image filtering followed by a subsequent automated thresholding.

Image filtering—Image filtering relies on a scale-space technique performed by an anisotropic diffusion process [35]. The initial distribution of gray levels $I(x,y,z,t = 0)$ is processed as a function of the scale-space parameter t by using:

$$I(x,y,z,t) = \text{div}[c(x,y,z,t) \times \text{grad}(I)] \quad (4)$$

$c(x,y,z,t)$ is defined in such way that the filtering (i) smoothes the gray levels within the phases and (ii) enhances the contrast at the region boundaries:

$$c(x,y,z,t) = \exp\left\{-\left(\|\text{grad}(I)\|/K\right)^2\right\} \quad (5)$$

where K is a constant adjusted in the present study to $K = 5$ for the filtering optimisation. A loop of 500 iterations on t is required to stabilise the processed image. Fig. 3(a) and (b) shows the brightness maps for a cross-section taken in the middle of the reconstructed Ni–8YSZ support before and after filtering. The associated gray-level distribution for the whole reconstruction is also plotted. It can be seen that the peaks of the distribution exhibit a better separation while the gray levels are more uniform within each phase.

Automated segmentation—The Otsu's method [36] for threshold determination is one of the most qualified methods for pores and electrodes materials segmentation [37]. In this approach, the gray levels are set in three clusters linked to each phase of the reconstruction:

$$\left\{ \sum_{i=0}^{i=K} p_i \right\} + \left\{ \sum_{i=K+1}^{i=M} p_i \right\} + \left\{ \sum_{i=M+1}^{i=255} p_i \right\} = 1 \quad \text{with } p_i = \frac{n_i}{N} \quad (6)$$

where n_i denotes the number of voxels at the gray level i and N is the total number of voxels. The term p_i corresponds to the probability that a voxel belongs to the level i . The total variance of the distribution σ_T^2 can be shared into a “within-class” variance σ_W^2 and a “between-class” variance σ_B^2 :

$$\sigma_T^2 = \sum_{i=0}^{i=255} (i - \mu_T)^2 p_i = \sigma_W^2 + \sigma_B^2 \quad \text{with } \mu_T = \sum_{i=0}^{i=255} i \times p_i \quad (7)$$

where μ_T represents the gray levels mean value calculated for the whole image. The first term σ_W^2 of eq. (7) is defined as the sum of the variances calculated for each cluster:

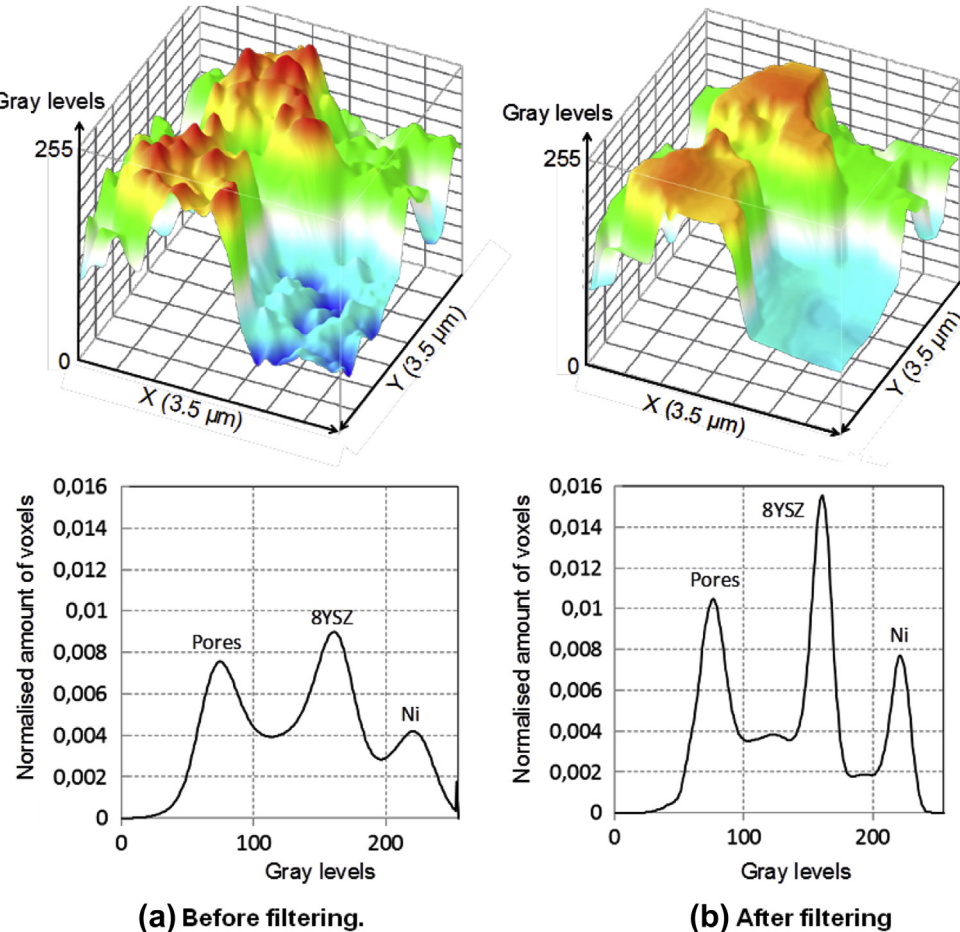


Fig. 3. Three-dimensional plot of the gray-levels brightness for a cross-section taken in the middle of the 3D reconstruction before and after the filtering. The associated grayscale frequency distribution for the whole reconstruction is also represented. The gray-level data correspond to the one recorded in the substrate of the electrode.

$$\begin{aligned} \sigma_W^2 &= \sum_{i=0}^{i=K} (i - \mu_{\text{pores}})^2 p_i + \sum_{i=K+1}^{i=M} (i - \mu_{\text{8YSZ}})^2 p_i + \sum_{i=M+1}^{i=255} (i - \mu_{\text{Ni}})^2 p_i \\ \text{with } \mu_{\text{pores}} &= \sum_{i=0}^{i=K} i \times p_i / \sum_{i=0}^{i=K} p_i \quad \mu_{\text{8YSZ}} = \sum_{i=K+1}^{i=M} i \times p_i / \sum_{i=K+1}^{i=M} p_i \\ \mu_{\text{Ni}} &= \sum_{i=M+1}^{i=255} i \times p_i / \sum_{i=M+1}^{i=255} p_i \end{aligned} \quad (8)$$

The second term σ_B^2 of eq. (7) is calculated considering the mean values of each class:

$$\begin{aligned} \sigma_B^2 &= \sum_{i=0}^{i=K} p_i (\mu_{\text{pores}} - \mu_T)^2 + \sum_{i=K+1}^{i=M} p_i (\mu_{\text{8YSZ}} - \mu_T)^2 \\ &+ \sum_{i=M+1}^{i=255} p_i (\mu_{\text{Ni}} - \mu_T)^2 \end{aligned} \quad (9)$$

The two thresholds K and M for image segmentation are determined so that the separation between the clusters is the highest. This criterion is equivalent to identifying the optimal thresholds K^* and M^* such as the “between-class” variance σ_B^2 is maximised according to:

$$\eta(K^*, M^*) = \max_{0 < K < M < 255} \frac{\sigma_B^2(K, M)}{\sigma_T^2} \quad \text{with } 0 \leq \eta \leq 1 \quad (10)$$

The parameter η provides an estimation of the reliability for the thresholding. It is equal to 0 if the gray-level distribution is uniform (i.e. without peaks and valleys) and equal to 1 if each phase is constituted by only one single gray level. Higher the indicator η is, better the segmentation. Indeed, if η is close to the unity, the “between-class” variance σ_B^2 tends toward σ_T^2 while the “within-class” variance σ_W^2 tends to zero. In this case, the ability to separate the classes is ideal.

After image filtering and segmentation, the volumetric fractions of each phase are simply determined as the ratio of the number of voxels belonging to a given phase over the total number of voxels. Furthermore, the mean particle diameters of each phase are extracted by the covariance method detailed in Ref. [23].

3. Results

Two large volumes of $51.2 \times 25.6^2 \times \pi \mu\text{m}^3$ were reconstructed from two nano-holotomography scans: the first one is centered on the AFL and the second one is located in the middle of the anode substrate. The voxel size is 25 nm, nevertheless the actual spatial resolution is about three pixels and depends on several factors (focal spot size, number of projections ...). Fig. 4 shows the

transverse and longitudinal cross-section phase contrast images of the holotomographic reconstruction centered on the AFL layer. Because of the large field of view, all the layers of the cell are apparent: the whole electrolyte and AFL layers are sandwiched between a part of the cathode and a part of the anode substrate. As expected, the AFL presents a thickness of $\sim 10 \mu\text{m}$ and exhibits a microstructure finer than the support.

In both the AFL and the anode substrate, the three different phases (pores/Ni/YSZ) are clearly discriminated and the 3D distribution of the three different phases in the anode of SOFC is observed on large reconstructed volume. As illustrated in Fig. 5, phase contrast images obtained on the sample with resin appear with better contrast and the region boundaries are sharper than the ones obtained without the resin. This improvement is due to the beneficial effect of the resin on the phase shift decrease.

The filtering and automated segmentation has been applied on data recorded for the two holotomography scans of the embedded sample. Figs. 6 and 7 show the 3D microstructures of the AFL and the support respectively. The volume fraction of each phase and the indicators η are summarised in Table 1. It can be noticed that the quality of the segmentation is high since the values of the threshold parameter η are close to the unity for both reconstructions.

It is worth mentioning that the pore fraction deduced from the reconstructed substrate is very similar to the one measured by Archimede's method (i.e. 47% as reported in Ref. [23]). Indeed, the difference between the two porosities is less than 1%. Moreover, the volumetric composition of the anode substrate in Ni and 8YSZ is found to be equal to 40.6 vol.%Ni and 59.4 vol.%8YSZ (cf. Table 1). This composition, which corresponds to a cermet constituted of 50.56 wt% Ni and 49.44 wt% 8YSZ, is very close to the values reported by the manufacturer (i.e. 50 wt% Ni and 50 wt% 8YSZ: see Section 2.1).

The values of mean particle diameter of Ni and YSZ and the pore size are reported in Table 2. Pores are on average three times smaller in the AFL and both Ni and YSZ mean diameters are about 30% lower in the functional layer. These results clearly show that

the microstructure is actually finer in the AFL compared to the support. These findings are well consistent with the features of the optimised cell microstructure reported by the manufacturer [38,39].

The good agreement with available average material properties allows expecting high accuracy from the three-dimensional reconstructions.

4. Discussion

In a previous work, holotomography has been already performed on SOFC anode with a pixel size of 60 nm, giving interesting results toward the porosity network but without distinction between the Ni and YSZ phases [23]. According to the considerations detailed in Ref. [40], the increase in the magnification (30 for 25 nm pixel size) coupled with an improvement of the contrast visibility has lead to a better discrimination of the phases. Moreover, the pore filling with resin has changed the Ni and YSZ phase contrast which has reached its optimum value: the refractive index decrement values of each phase have been measured on the reconstructed images and are found to be close to their theoretical values.

The reconstructed volumes (i.e. $51.2 \times 25.6^2 \times \pi \mu\text{m}^3$ in the substrate and $10 \times 25.6^2 \times \pi \mu\text{m}^3$ in the AFL) seem to be large enough to be statistically representative for the heterogenous ACC and AFL. In the one hand, it can be noticed that the size of these reconstructions is much larger than the RVEs found in the previous studies ($\sim 35 \times 35 \times 35 \mu\text{m}^3$ for ACC [23] and $\sim 10 \times 10 \times 10 \mu\text{m}^3$ for AFL [16]). In a previous work performed on the same electrode microstructure, it has been demonstrated [23] that the RVE size corresponding to the phases' percentage is equal to the one for the tortuosity factor. Hereafter, we only refer to this RVE corresponding to morphological properties. In the other hand, the theoretical representative volumes of the two studied reconstructions can be estimated through the rule proposed by Metcalfe et al. [41] and verified by Laurencin et al. [23]. Indeed, on synthetic

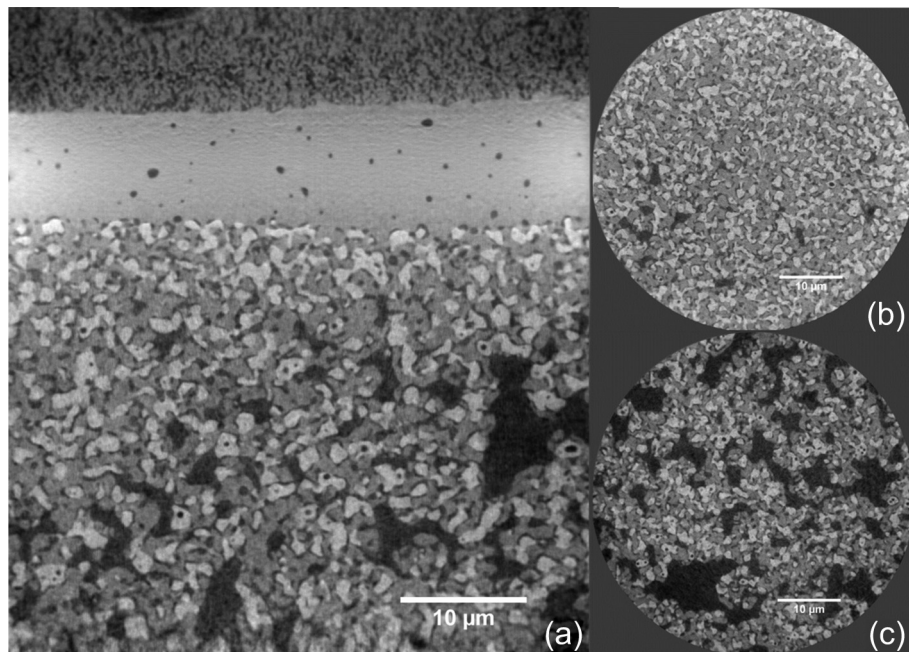


Fig. 4. (a) Longitudinal cross-section of the 25 nm pixel size holotomography reconstruction (with epoxy resin). It shows four layers of the cell: a part of the cathode, the electrolyte, the AFL and the anode substrate. (b) Transverse cross-section in the AFL part. (c) Transverse cross-section in the anode substrate part. In all the reconstructions the gray-level scales proportionally with the electron density of the material i.e. phase contrast images. The pores appear in dark, the YSZ in gray and the nickel is the whiter phase.

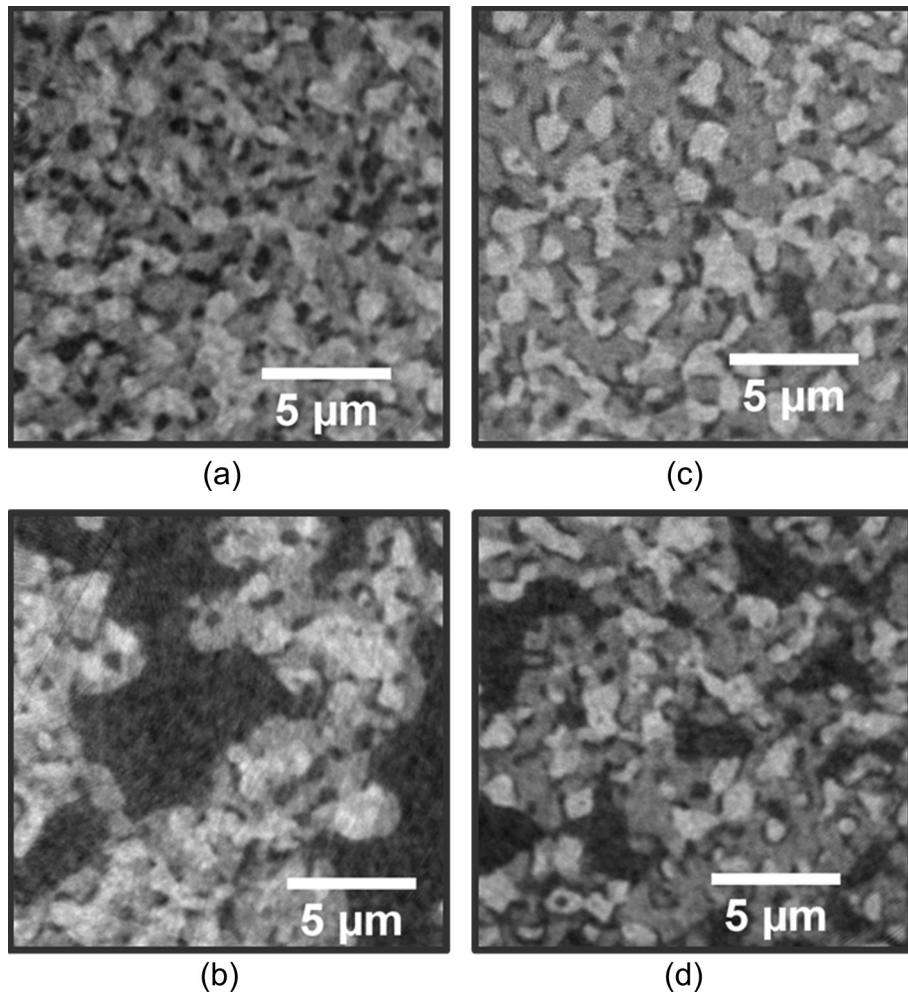
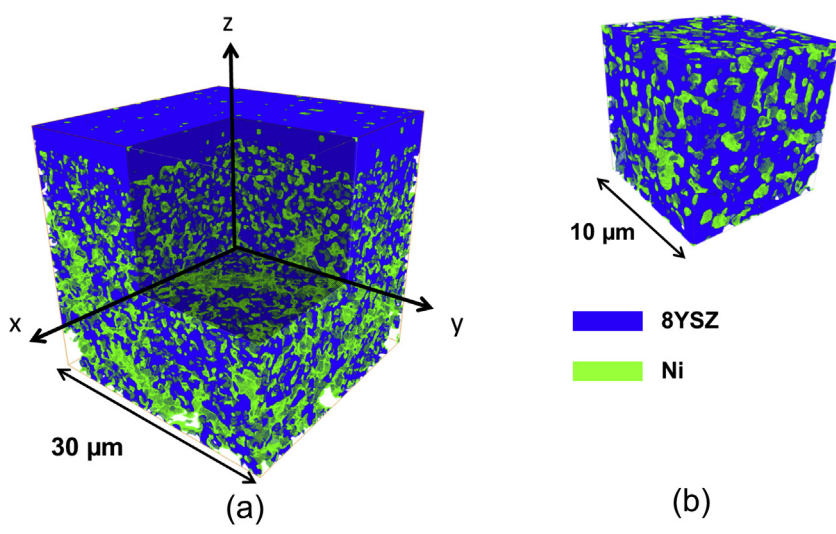


Fig. 5. Comparison of microstructure details between the cell without epoxy resin embedding (a) in the AFL and (b) in the anode substrate and the cell with epoxy resin embedding (c) in the AFL and (d) in the anode substrate. Every reconstruction is a phase contrast image in which the pores appear in dark, the YSZ in gray and the nickel is the whiter phase.



(a) Volume of $30 \times 30 \times 30 \mu\text{m}^3$ including the electrolyte, the functional layer and a part of the substrate.

(b) Zoom on the functional layer ($10 \times 10 \times 10 \mu\text{m}^3$).

Fig. 6. Illustration of the three-dimensional reconstructed microstructure including the Ni/8YSZ functional layer. The rendered volumes have been taken in the middle of the whole reconstruction.

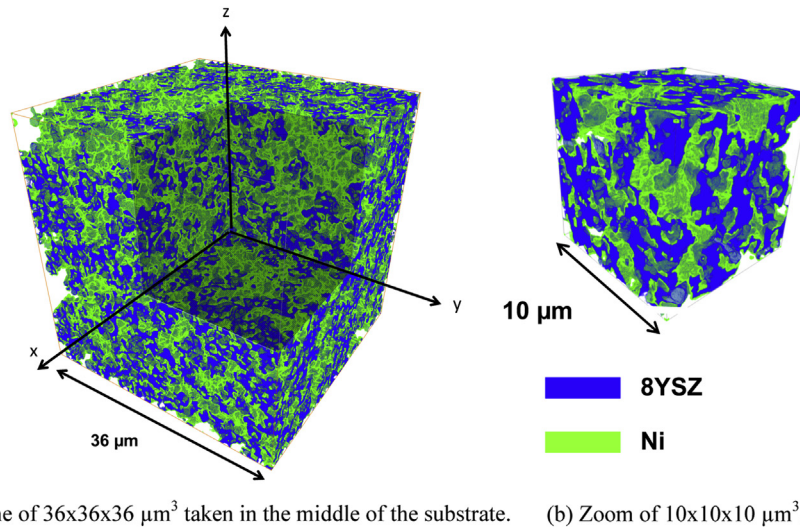


Fig. 7. Illustration of the three-dimensional reconstructed microstructure for the Ni–8YSZ support. The rendered volumes have been taken in the middle of the whole reconstruction.

Table 1

Volume fraction of pores, Ni and 8YSZ phases. The indicator η of thresholding quality is also given.

3D reconstruction	Pores (vol.%)	8YSZ (vol.%)	Ni (vol.%)	η
Substrate	46.6	31.7	21.7	0.912
Functional layer	22.8	49.0	28.2	0.904

microstructure, Metcalfe et al. [41] have claimed that the “cubic envelope of the reconstruction must have a length of 14 times the mean particle diameter”. In order to obtain an upper bound for RVE, this rule has been applied by using the highest value among the Ni, 8YSZ and pores mean diameters. As reported in Table 2, it is found that the size of the RVE is roughly equal to $\ell_{\text{RVE}}^{\text{ACC}} \approx 36 \mu\text{m}$ for the anode substrate and $\ell_{\text{RVE}}^{\text{AFL}} \approx 13 \mu\text{m}$ for the AFL. As a consequence, the proposed X-ray nano-holotomography methodology allows obtaining volumes especially relevant for both the substrate and the functional layer analysis.

Joos et al. [37,42] have estimated the adequate resolution to obtain trustworthy results. By a purely numerical analysis on synthetic microstructure that mimic Lanthane Strontium Cobalt Iron oxide electrode (LSCF), the authors have shown that ~ 15 [42] or ~ 20 [37] voxels per particle diameter are required to converge to the theoretical value of surface area. To determine a lower bound of the required voxel size, this rule has been applied by considering the lowest value among the Ni, 8YSZ and pores mean diameters. As reported in Table 2, it is found that a voxel size of ~ 55 nm is sufficient to accurately describe the coarse microstructure of the substrate; whereas a voxel size of ~ 36 nm is necessary for the fine

microstructure of the functional layer. This last result is in good agreement with the Holzer et al. statement [11]. Indeed the authors reported for similar microstructures that “resolutions better than 35 nm are sufficient for reproducible particles size measurements”. Therefore, the voxel size of 25 nm obtained with our experimental conditions is well adapted to obtain accurate results in both the substrate and the functional layer.

Thus, the combination of a small voxel size and a large volume of our three-dimensional reconstructions (i.e. $51.2 \times 25.6^2 \times \pi = 105,414 \mu\text{m}^3$ with $\ell_{\text{voxel}} = 25 \text{ nm}$) allows them to be highly representative of both the functional layer and the anode support. These characteristics can be favorably compared to the current state of the art. Indeed, to our best knowledge, it is the first time that such combination of small voxel size and large analysed volume is obtained. For instance, by FIB-SEM tomography, Kanno et al. [24] have obtained a reconstructed volume of $48.5 \times 14.5 \times 26.2 = 18,425 \mu\text{m}^3$ with a voxel size of 55.8 nm; while Chen-Wiegart et al. [43] by X-ray tomography have recently achieved a reconstructed volume of $\sim 3600 \mu\text{m}^3$ with a voxel size of 45 nm. This improvement compared to the previous analyses using nanotomography is brought by a high X-ray energy (29 keV while the energy previously used is around the Ni K-absorption edge: 8.333 keV [14,17–19,21,44]).

The 3D reconstructions are now available to calculate with a good confidence the effective properties such as the tortuosity factors, TPB length, etc. This work is on going on the functional layer and the support and will be published soon in a separate paper.

More generally, this technique can be used to investigate many other microstructures of porous or multi-phased materials like bones, metallic foam or alloys with the following advantages: (i) it is a non-destructive technique, which makes it possible to combine X-ray tomography with other techniques or follow the evolution of the microstructure, (ii) large volumes can be analysed with high accuracy and (iii) it allows discriminating several phases.

5. Conclusion

Three-dimensional tomography at 25 nm voxel size has been demonstrated on an SOFC anode. Our contribution highlights (i) the specific sample preparation for X-ray nano-holotomography of SOFC samples with cross-section as large as 100 μm , (ii) the importance of using hard X-rays, in our case an energy of 29 keV,

Table 2

Particles mean diameter D_p and size of the RVE ℓ_{RVE} estimated according to Metcalfe et al. [41] postulate. The adequate image resolution is estimated according the rule given by Joos et al. [37,42].

3D reconstruction	Mean diameter D_p (μm)			Accurate resolution (nm)	ℓ_{RVE} (μm)
	Gas phase	Ni phase	8YSZ phase		
Substrate	2.6	1.2	1.1	$D_p^{\text{8YSZ}}/20 \approx 55$	$14 \times D_p^{\text{gas}} \approx 36$
Functional layer	0.94	0.83	0.73	$D_p^{\text{8YSZ}}/20 \approx 36$	$14 \times D_p^{\text{gas}} \approx 13$

(iii) the feasibility of high-Z material 3D nano-imaging with an improved phase retrieval scheme and optimised phase retrieval conditions by embedding the materials into resin, (iv) the specific filtering and thresholding for the images segmentation and (v) the success in imaging a sample whose cross-section is twice the field of view. On top of that, it must be mentioned that such 3D images could not be obtained without the use of 3rd generation synchrotron because of both brilliance and hard X-ray requirements.

In this work, a set of high resolution tomography acquisitions have been performed on the AFL and on anode substrate revealing interesting features of their complex microstructure. Three-dimensional networks of each phase (pores, Ni and YSZ) have been reconstructed over a volume large enough, i.e. larger than the RVE of this material. Morphological details of each phase ranging from 25 nm to 51.2 μm are supplied which fulfills the requirements for analysing the anode microstructure. The original methodology presented here considerably increases the representativeness of the 3D reconstructions from which more realistic simulation of physical processes can be expected.

Acknowledgment

The authors would like to thanks J.M. Fabbri and B. Florin from Leti-Minatec for the efficient management of the challenging SOFC sample preparation.

References

- [1] A.J. Jacobson, *Chem. Mater.* 22 (2012) 660–674.
- [2] Y. Harumi, T. Hengyong, B. Iwanschitz, M. Andreas, *J. Power Sources* 182 (2008) 400–412.
- [3] X. Liu, C.L. Martin, G. Delette, J. Laurencin, D. Bouvard, T. Delahaye, *J. Power Sources* 196 (4) (2011) 2046–2054.
- [4] D. Simwonis, F. Tietz, D. Stöver, *Solid State Ionics* 132 (2000) 241–251.
- [5] A. Bertei, C. Nicollella, *J. Power Sources* 196 (2011) 9429–9436.
- [6] J. Laurencin, G. Delette, O. Sicardi, S. Rosini, F. Lefebvre-Joud, *J. Power Sources* 195 (2010) 2747–2753.
- [7] J.R. Wilson, J.S. Cronin, S.A. Barnett, *Scr. Mater.* 65 (2) (2011) 67–72.
- [8] H. Iwai, N. Shikazono, et al., *J. Power Sources* 195 (4) (2010) 955–961.
- [9] J. Malzbender, R.W. Steinbrech, L. Singheiser, *Fuel Cells* 6 (2009) 785–793.
- [10] Z.J. Jiao, N. Shikazono, N. Kasagi, *J. Electrochem. Soc.* 159 (3) (2012) B285–B291.
- [11] L. Holzer, B. Münch, B. Iwanschitz, M. Cantoni, Th. Hocker, Th. Graule, *J. Power Sources* 196 (2011) 7076–7089.
- [12] P.R. Shearing, D.J.L. Brett, N.P. Brandon, *Int. Mater. Rev.* 55 (6) (2010) 347–363.
- [13] J.R. Wilson, W. Kobsiriphat, et al., *Nat. Mater.* 5 (2006) 541–544.
- [14] Y. Guan, Y.H. Gong, W.J. Li, J. Gelb, L. Zhang, G. Liu, X.B. Zhang, X. Song, C. Xia, Y. Xiong, H.Q. Wang, H. Wang, W.B. Yun, Y.C. Tian, *J. Power Sources* 196 (2011) 10601–10605.
- [15] N. Vivet, S. Chupin, E. Estrade, A. Richard, S. Bonnamy, D. Rochais, E. Bruneton, *J. Power Sources* 196 (2011) 7541–7549.
- [16] J.S. Cronin, J.R. Wilson, S.A. Barnett, *J. Power Sources* 196 (2011) 2640–2643.
- [17] K.N. Grew, Y.S. Chu, J. Yi, A.A. Peracchio, J.R. Izzo, Y. Hwu, F. De Carlo, W.K.S. Chiu, *J. Electrochem. Soc.* 157 (6) (2010) B783–B792.
- [18] P.R. Shearing, J. Gelb, J. Yi, W.-K. Lee, M. Drakopoulous, N.P. Brandon, *Electrochim. Commun.* 12 (2010) 1021–1024.
- [19] G.J. Nelson, J.R. Izzo, J.J. Lombardo, W.M. Harris, A.P. Cocco, W.K.S. Chiu, K.N. Grew, A. Faes, A. Hessler-Wyser, J. Van Herle, Y.S. Chu, S. Wang, *ECS Trans.* 35 (1) (2011) 1323–1327.
- [20] P.R. Shearing, R.S. Bradley, J. Gelb, S.N. Lee, A. Atkinson, P.J. Withers, N.P. Brandon, *Electrochim. Solid-State Lett.* 14 (10) (2011) B117–B120.
- [21] G.J. Nelson, K.N. Grew, J.R. Izzo, J.J. Lombardo, W.M. Harris, A. Faes, A. Hessler-Wyser, J. Van Herle, S. Wang, Y.S. Chu, A.V. Virkar, W.K.S. Chiu, *Acta Mater.* 60 (2012) 3491–3500.
- [22] P.R. Shearing, Q. Cai, J.I. Golbert, V. Yufit, C.S. Adjiman, N.P. Brandon, *J. Power Sources* 195 (2010) 4804–4810.
- [23] J. Laurencin, R. Quey, G. Delette, H. Suhonen, P. Cloetens, P. Bleuet, *J. Power Sources* 198 (2012) 182–189.
- [24] D. Kanno, N. Shikazono, N. Takagi, K. Matsuzaki, N. Kasagi, *Electrochim. Acta* 56 (2011) 4015–4021.
- [25] J.R. Wilson, J.S. Cronin, A.T. Duong, S. Rukes, H.-Y. Chen, K. Thornton, D.R. Mumm, S. Barnett, *J. Power Sources* 195 (2010) 1829–1840.
- [26] P.R. Shearing, J. Golbert, R.J. Chater, N.P. Brandon, *Chem. Eng. Sci.* 64 (2009) 3928–3933.
- [27] J. Gelb, W.B. Yun, M. Feser, A. Tkachuk, D.G. Seiler, A.C. Diebold, R. McDonald, C.M. Garner, D. Herr, R.P. Khosla, E.M. Secula, *Frontiers of characterization and metrology for nanoelectronics: X-ray microscopy for interconnect characterization*, AIP Conf. Proc. 1173 (2009) 145–148.
- [28] R.N. Basu, G. Blass, H.P. Buchkremer, D. Stöver, F. Tietz, E. Wessel, I.C. Vinke, *J. Eur. Ceram. Soc.* 25 (2005) 463–471.
- [29] G. Martinez-Criado, R. Tucoulou, P. Cloetens, P. Bleuet, S. Bohic, J. Cauzid, I. Kieffer, E. Kosior, S. Laboure, S. Petitgirard, A. Rack, J.A. Sans, J. Segura-Ruiz, H. Suhonen, J. Susini, J. Villanova, *J. Synchrotron Rad.* 19 (2012) 10–18.
- [30] P. Cloetens, W. Ludwig, J. Baruchel, D. Van Dyck, J. Van Landuyt, J.-P. Guigay, M. Schlenker, *Appl. Phys. Lett.* 75 (1999) 2912–2914.
- [31] G. Requena, P. Cloetens, W. Altendorfer, C. Poletti, D. Tolnai, F. Warchomicka, H. Degischer, *Scr. Mater.* 61 (2009) 760–763.
- [32] B.L. Henke, E.M. Gullikson, J.C. Davis, *Atom. Data Nucl. Data* 54 (2) (1993) 181–342.
- [33] H.F. Talbot, *Philos. Mag.* 9 (1836) 401–407.
- [34] D.M. Paganin, *Coherent X-Ray Optics*, In: Oxford Series on Synchrotron Radiation, Vol. 6, Oxford University Press, Oxford, 2006.
- [35] P. Perona, J. Malik, *IEEE Trans. Pattern Anal. Machine Intel.* 12 (7) (1990) 629–639.
- [36] N. Otsu, *IEEE Trans. Syst. Man Cybernetics, SMC* 9 (1) (1979) 62–66.
- [37] J. Joos, T. Carraro, A. Weber, E. Ivers-Tiffée, *J. Power Sources* 196 (17) (2011) 7302–7307.
- [38] F. Tietz, H.P. Buchkremer, D. Stöver, *J. Electroceram.* 17 (2006) 701–707.
- [39] N.H. Menzler, S. Uhlenbruck, H.P. Buchkremer, D. Stöver, *J. Mater. Sci.* 45 (2010) 3109–3135.
- [40] A. Beerlink, S. Thutupalli, M. Mell, M. Bartels, P. Cloetens, S. Herminghaus, T. Salditt, *Soft Matter* 8 (2012) 4595–4601.
- [41] C. Metcalfe, O. Kesler, T. Rivard, F. Gitzhofer, N. Abatzoglou, *J. Electrochim. Soc.* 157 (9) (2010) B1326–B1335.
- [42] J. Joos, M. Ender, T. Carraro, A. Weber, E. Ivers-Tiffée, *Electrochim. Acta* (2012) 10–15.
- [43] Yu-chen Karen Chen-Wiegart, J. Scott Cronin, Qingxi Yuan, Kyle J. Yakal-Kremski, Scott A. Barnett, Jun Wang, *J. Power Sources* 218 (2012) 348–351.
- [44] Y. Guan, W. Li, Y. Gong, G. Liu, X. Zhang, J. Chen, J. Gelb, W. Yun, Y. Xiong, Y. Tian, H. Wang, *J. Power Sources* 196 (2011) 1915–1919.